

# The kinematics of $\sigma$ -drop bulges from spectral synthesis modelling of a hydrodynamical simulation

Elisa Portaluri,<sup>1\*</sup> Victor P. Debattista,<sup>2</sup> Maximillian Fabricius,<sup>3,4</sup> David R. Cole,<sup>5</sup>  
Enrico M. Corsini,<sup>6,1</sup> Niv Drory,<sup>7</sup> Andrew Rowe,<sup>8</sup> Lorenzo Morelli,<sup>6,1</sup>  
Alessandro Pizzella,<sup>6,1</sup> and Elena Dalla Bontà<sup>6,1</sup>

<sup>1</sup>*INAF–Osservatorio Astronomico di Padova, Vicolo dell’Osservatorio 2, I-35122 Padova, Italy*

<sup>2</sup>*Jeremiah Horrocks Institute, University of Central Lancashire, Preston, PR1 2HE, UK*

<sup>3</sup>*Max-Planck-Institut für extraterrestrische Physik, Giessenbachstraße, D-85748 Garching, Germany*

<sup>4</sup>*Universitäts-Sternwarte München, Scheinerstraße 1, D-81679 München, Germany*

<sup>5</sup>*Rudolf Peierls Centre for Theoretical Physics, Keble Road, Oxford, OX1 3NP, UK*

<sup>6</sup>*Dipartimento di Fisica e Astronomia ‘G. Galilei’, Università di Padova, vicolo dell’Osservatorio 3, 35122 Padova, Italy*

<sup>7</sup>*Department of Astronomy, The University of Texas at Austin, 2515 Speedway, Stop C1400, Austin, TX 78712, USA*

<sup>8</sup>*Materials and Physics Research Centre, University of Salford, Salford, M5 4WT, UK*

Accepted xxx Received xxx ; in original form 28 August 2021

## ABSTRACT

A minimum in stellar velocity dispersion is often observed in the central regions of disc galaxies. To investigate the origin of this feature, known as a  $\sigma$ -drop, we analyse the stellar kinematics of a high-resolution  $N$ -body + smooth particle hydrodynamical simulation, which models the secular evolution of an unbarred disc galaxy. We compared the intrinsic mass-weighted kinematics to the recovered luminosity-weighted ones. The latter were obtained by analysing synthetic spectra produced by a new code, SYNTRA, that generates synthetic spectra by assigning a stellar population synthesis model to each star particle based on its age and metallicity. The kinematics were derived from the synthetic spectra as in real spectra to mimic the kinematic analysis of real galaxies. We found that the recovered luminosity-weighted kinematics in the centre of the simulated galaxy are biased to higher rotation velocities and lower velocity dispersions due to the presence of young stars in a thin and kinematically cool disc, and are ultimately responsible for the  $\sigma$ -drop.

Our procedure for building mock observations and thus recovering the luminosity-weighted kinematics of the stars in a galaxy simulation is a powerful tool that can be applied to a variety of scientific questions, such as multiple stellar populations in kinematically-decoupled cores and counter-rotating components, and galaxies with both thick and thin disc components.

**Key words:** galaxies: bulges — galaxies: evolution — galaxies: kinematics and dynamics — galaxies: nuclei — galaxies: stellar content — galaxies: structure

## 1 INTRODUCTION

The stellar velocity dispersion in many nearby galaxies exhibits a central drop rather than a peak (Emsellem et al. 2001; Comerón et al. 2008; Krajnović et al. 2013). Such a  $\sigma$ -drop was first predicted by Binney (1980) and subsequently shown to be a common property of galaxies with a surface brightness distribution following a Sérsic profile (Ciotti & Lanzoni 1997).

The first  $\sigma$ -drops were detected by Jarvis et al. (1988) in a sample of SB0 galaxies. Afterwards, this feature was detected in the late-type spiral galaxy NGC 6503 by Bottema (1989), who in-

terpreted it as due to a central dip in the vertical velocity dispersion.  $\sigma$ -drops are known to be a widespread feature of the stellar kinematics in the centre of both quiescent and active galaxies. They are observed in approximately 30% of early-type (Graham et al. 1998; Krajnović et al. 2008) and 40% of spiral galaxies (Chung & Bureau 2004; Falcón-Barroso et al. 2006). This fraction rises to about 70% for barred galaxies (Pérez, Sánchez-Blázquez, & Zurita 2009; Méndez-Abreu et al. 2014).

Koleva et al. (2008) pointed out that a metallicity mismatch of the spectral library adopted in measuring the stellar kinematics may bias the central velocity dispersion to lower values, producing spurious  $\sigma$ -drops where none exist. As a consequence, the fraction of  $\sigma$ -drop galaxies may be overestimated. However, state-

\* E-mail: elisa.portaluri@oapd.inaf.it

of-the-art methods for measuring stellar kinematics are designed to deal with a metallicity mismatch (e.g. Cappellari & Emsellem 2004; Koleva et al. 2008; Fabricius et al. 2014) and  $\sigma$ -drops have been measured using a variety of techniques, spectral libraries and wavelength ranges, suggesting that a template mismatch is not the cause of most  $\sigma$ -drops.

The origin and nature of  $\sigma$ -drops are particularly important for disc galaxies. Being related to the structure of the bulge component and to the central mass distribution,  $\sigma$ -drops can be used to discriminate between the different types of bulges. Classical bulges show centrally peaked velocity dispersion profiles, whereas  $\sigma$ -drops are usually observed in pseudobulges and composite bulges, which are characterized by different components coexisting in the same structure (Fabricius et al. 2012; Méndez-Abreu et al. 2014; Erwin et al. 2015). In addition,  $\sigma$ -drops are often associated with nuclear dust spirals and nuclear star-forming rings (Comerón et al. 2008) while their extent does not depend on the bulge (Méndez-Abreu et al. 2014) or galaxy size (Comerón et al. 2008).

Different mechanisms have been proposed to explain how  $\sigma$ -drops form and develop. Simple dynamical models based on the epicyclic theory are not able to explain the stellar kinematics in the central regions of  $\sigma$ -drop galaxies (Bottema & Gerritsen 1997; Emsellem et al. 2001), suggesting that the decrease in velocity dispersion is due to a cold nuclear disc with recent star formation fueled by gas inflows. The stars of the nuclear disc have almost the same kinematics as the gas from which they formed, so their velocity dispersion is lower than that of the older surrounding stars. The measured kinematics are biased to the lower velocity dispersion of the younger stars since they outshine the older stellar populations. Such a scenario has been investigated by hydrodynamical simulations (Wozniak et al. 2003; Wozniak & Champavert 2006). In their simulations the  $\sigma$ -drop forms in less than 500 Myr, but its lifetime can exceed 1 Gyr if the nuclear region is continuously fed with gas to sustain star formation at a level of about  $1 M_{\odot} \text{ yr}^{-1}$ . This easily occurs in gas-rich spiral galaxies where a bar funnels gas towards the centre. This model explains why  $\sigma$ -drop galaxies may host an inner dust system of spiral arms that traces the path of the inflowing material. Galaxies with a  $\sigma$ -drop show inner rings or nuclear discs. The same mechanism that feeds the nuclear structures is probably responsible for the higher fraction of Seyfert galaxies among  $\sigma$ -drop galaxies (Comerón et al. 2008). Using dissipationless simulations, Athanassoula & Misiriotis (2002) and Bureau & Athanassoula (2005) proposed an alternative scenario where a massive and concentrated dark matter halo removes kinetic energy from the stellar component in the nuclear region, causing a reduction in the velocity dispersion and the formation of a strong bar. Another possibility is that the central  $\sigma$ -drop is the signature of a nuclear bar counter-rotating with respect to the main bar of the galaxy (Friedli 1996).

The fact that  $\sigma$ -drops are observed in unbarred galaxies leads to the conclusion that bars may not always play a role. de Lorenzo-Cáceres et al. (2012) showed that a  $\sigma$ -drop is the signature of the presence of a pseudobulge, which has disc properties and thus a lower velocity dispersion with respect to the rest of the galaxy. In this case, the  $\sigma$ -drop is not actually a drop with respect to the higher velocity dispersion of the bulge, but the maximum velocity dispersion of the pseudobulge itself. Alternatively, the kinematics of galaxies hosting counter-rotating stellar discs is characterized by two off-centre and symmetric peaks in the stellar velocity dispersion in combination with zero velocity rotation measured along the galaxy major axis. These kinematic features, which result in a remarkably strong  $\sigma$ -drop, are observed in the radial range where

the two counter-rotating components have roughly the same luminosity and their line-of-sight velocity distributions (LOSVDs) are unresolved (Bertola et al. 1996; Coccato et al. 2015). Other studies interpreted the presence of the  $\sigma$ -drop as due to the lack of a central supermassive black hole or more generally of a flat density core (Dressler & Richstone 1990). Other authors suggest that  $\sigma$ -drops are due to an underestimation of the true velocity dispersion in galaxies hosting a central supermassive black hole (van der Marel 1994).

In this paper, we study the kinematic properties of a simulated bulge characterized by a  $\sigma$ -drop, using a hydrodynamical simulation of an unbarred spiral galaxy combined with stellar population synthesis models. We compare the intrinsic kinematics of the stellar component we measure directly from the simulation to the one we recover by mimicking real integral-field spectroscopic observations. The simulation is presented in Section 2 and the analysis method of the intrinsic mass-weighted and recovered luminosity-weighted stellar kinematics of the simulated galaxy is presented in Section 3. The results are discussed in Section 4 and conclusions are given in Section 5.

## 2 SIMULATION

The simulation we use here is similar to the model presented in Cole et al. (2014). The model forms a disc galaxy inside a pressure-supported gas corona within a dark matter halo. The host dark matter halo has a virial radius  $r_{200} = 198$  kpc, virial mass  $M_{200} = 9 \times 10^{11} M_{\odot}$  and concentration  $c = 19$ . Both the dark matter halo and the initial gas corona consist of 5 million particles. The dark matter particles have mass  $8.5 \times 10^4 M_{\odot}$  (those with starting radius smaller than 56 kpc, corresponding to 90% of the halo particles), while those at larger radii have a mass  $1.7 \times 10^6 M_{\odot}$ . Dark matter particles have a softening  $\epsilon = 103$  pc. Gas particles have softening  $\epsilon = 50$  pc, inherited by star particles forming from them; initially gas particles all have mass  $2.7 \times 10^4 M_{\odot}$ , giving the corona a mass 11% that of the dark matter. The gas corona has an initial angular momentum such that  $\lambda = 0.041$ . The initial conditions do not include star particles, all of which form from the gas as it cools and settles into a disc.

The simulation was evolved with the  $N$ -body+smoothed-particle hydrodynamics (SPH) code GASOLINE (Wadsley, Stadel, & Quinn 2004) with an opening angle of the tree code  $\theta = 0.7$ . We use a base time step of 10 Myr with a refinement parameter  $\eta = 0.175$ ; gas particles also satisfy the time step condition  $\delta t_{\text{gas}} = \eta_{\text{courant}} h / [(1 + \alpha)c + \beta \mu_{\text{max}}]$ , where  $h$  is the SPH smoothing length,  $\alpha$  is the shear coefficient, which is set to 1, the viscosity coefficient  $\beta = 2$  and  $\mu_{\text{max}}$  is described in Wadsley, Stadel, & Quinn (2004).  $\eta_{\text{courant}} = 0.4$  is the refinement parameter for gas particles and controls their time step size. The SPH kernel uses the 32 nearest neighbours. We use the gas cooling, star formation and stellar feedback prescriptions of Stinson et al. (2006), which do not take into account the effect of gas metallicity.

A gas particle is eligible to form stars if it has number density  $n > 100 \text{ cm}^{-3}$ , is cooler than  $T = 15,000$  K and is part of a converging flow. However only 10% of eligible gas particles actually form stars; these form with a mass  $9.4 \times 10^3 M_{\odot}$ . A gas particle can form multiple star particles but if its mass falls below 21% of the initial mass then its remaining mass is distributed amongst the nearest neighbours, and the particle deleted.

Each star particle corresponds to a stellar population with a Miller-Scalo (Miller & Scalo 1979) initial mass function. Stellar

feedback from Type II and Type Ia supernovae (SNeII, SNeIa) is included, as well as from AGB stellar winds. The effect of the supernova feedback, which deposits  $0.4 \times 10^{51}$  erg of energy per supernova, is modelled at the subgrid level as a blast wave through the interstellar medium (Stinson et al. 2006). GASOLINE tracks the production of iron and oxygen using the yields of Raiteri, Villata, & Navarro (1996); Woosley & Weaver (1995) and Weidemann (1987). Unlike the simulation in Cole et al. (2014), metallicity diffusion (*e.g.* Loebman et al. 2011) between gas particles was included in this simulation with the diffusion parameter of Shen et al. (2010) set to  $D = 0.03$ . We do not include any AGN feedback since the model does not contain a supermassive black hole.

### 3 INTRINSIC MASS-WEIGHTED AND RECOVERED LUMINOSITY-WEIGHTED KINEMATICS

In this paper we generate mock observations by building spectra from the available simulation time-steps. We consider only the star particles of the simulated galaxy and neglect the contribution of gas particles to the resulting luminosity-weighted spectra, which we analyse as if they were real, using standard data-analysis techniques. The recovered stellar kinematics are compared with the intrinsic ones obtained by weighting the velocity of the star particles by their mass.

The mock spectra are generated using SYNTRA (*i.e.* SYNthetic specTRA) our code written in the PYTHON language was designed specifically to select stellar population synthesis models to assign the spectral energy distribution suitable to each star particle of the simulation time-step according to its age and metallicity and produce final spectra with a given instrumental setup. We use the GALAXEV library of evolutionary stellar population synthesis models computed using the isochrone synthesis code of Bruzual & Charlot (2003). They cover the wavelength range from 3200 Å to 9500 Å with a resolution of 3 Å and were obtained using the evolutionary tracks by Bertelli et al. (1994) adopting a Salpeter (1995) initial mass function with a lower and upper mass cutoff of 0.1 and 100  $M_{\odot}$ , respectively. As we do not have a stellar population synthesis model for all the combinations of ages and metallicities of the star particles, SYNTRA considers the bins listed in Table 1 to assign the stellar population synthesis model to each star particle.

The adopted stellar population models are shifted according to the line-of-sight (LOS) velocities of the star particles and weighted by their luminosities. We add Poissonian noise to the single mock spectra but we did not include either read-out or background noise. Finally, the star particles are grouped into  $71 \times 71$  apertures of  $0.15 \times 0.15$  kpc<sup>2</sup> in the galaxy plane and their single mock spectra are summed, generating a number of luminosity-weighted spectra. They are then rebinned along the dispersion direction to a logarithmic scale with a binning in velocity corresponding to the spectral resolution of the stellar population models (22 km s<sup>-1</sup>). This allows SYNTRA to build a mock integral-field spectroscopic data cube for each simulation time-step that covers the inner  $5.3 \times 5.3$  kpc<sup>2</sup> of the simulated galaxy for a given orientation.

The measurement of the stellar kinematics from spectra is usually done by matching an observed spectral region where absorption lines are present with a set of template spectra of either observed stars or stellar population synthesis models at the same instrumental spectral resolution. The relative broadening between the observed and template spectrum then gives the galaxy

**Table 1.** Age and metallicity bins used for the spectral synthesis.

Range (1)	Adopted Value (2)
Age (10 <sup>9</sup> Gyr)	
0.025 - 0.075	0.050
0.075 - 0.150	0.100
0.150 - 0.300	0.200
0.300 - 0.500	0.400
0.500 - 0.700	0.570
0.700 - 0.900	0.810
0.900 - 1.200	1.020
1.200 - 1.600	1.430
1.600 - 2.250	2.000
2.250 - 2.750	2.500
2.750 - 3.500	3.000
3.500 - 4.500	4.000
4.500 - 5.500	5.000
5.500 - 7.000	6.000
7.000 - 9.000	8.000
9.000 - 11.000	10.000
11.000 - 20.000	13.000
Z (dex)	
0.0000 - 0.0002	0.0001
0.0002 - 0.0020	0.0004
0.0020 - 0.0060	0.0040
0.0060 - 0.0140	0.0080
0.0140 - 0.0350	0.0200
0.0350 - 1.0000	0.0500

*Note.* Column (1): age and metallicity bins of the simulation star particles. Column (2): adopted age and metallicity for the stellar population synthesis model from (Bruzual & Charlot 2003).

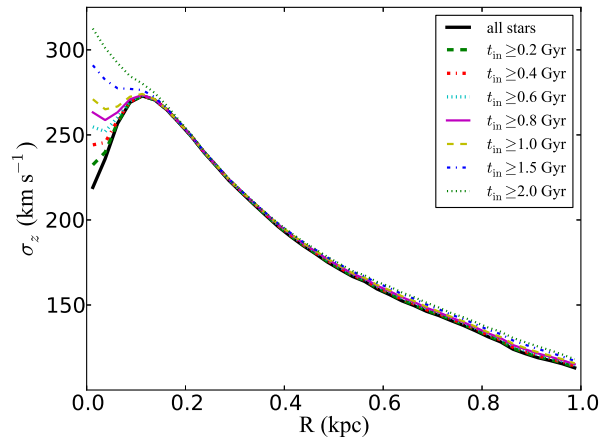


**Figure 1.** Radial profile of the vertical velocity dispersion  $\sigma_z$  measured from the intrinsic mass-weighted kinematics as a function of the age of the simulation star particles. This is the azimuthal average profile along the  $z$ -direction with respect to the plane of the galaxy at 10 Gyr, as seen face-on. The solid black line corresponds to the profile obtained including all the simulation star particles while the coloured lines from bottom to top show to the profiles obtained without stars younger than 0.2, 0.4, . . . , 1.0, 1.5 and 2.0 Gyr as indicated in the top-right corner. A colour version of this figure is available online.

velocity dispersion. We use the penalized pixel-fitting algorithm (pPXF, Cappellari & Emsellem 2004) with the GALAXEV library to recover the luminosity-weighted stellar kinematics from the absorption lines of the mock spectra in the wavelength ranges between 4750 Å and 5250 Å, which covers the Mg I triplet at  $\lambda$  5164, 5173, 5184 Å and between 8300 Å and 8800 Å covering the Ca II triplet at  $\lambda$  8498, 8542, 8662 Å. The pPXF algorithm applies the maximum penalized likelihood method to extract information from observed galaxy spectra. It works in pixel space creating the model galaxy spectrum by convolving a template spectrum with a Gauss-Hermite parametrized LOSVD (van der Marel & Franx 1993; Gerhard 1993). The Gauss-Hermite moments are an effective measure of the velocity distribution of a galaxy due to the Gaussian nature of the first order term in the expansion of the LOSVD. The first moment is related to the average LOS velocity,  $v$ , of a collection of stars within a galaxy while the second moment is the variance of the first moment and therefore is related to the LOS velocity dispersion,  $\sigma$ . A  $\chi^2$  analysis shows that this parametrization is satisfactory for measuring the LOSVD of the simulated galaxy and that the wide range of age and metallicity covered by models available in the GALAXEV library at least minimizes the effect of template mismatching in measuring the stellar kinematics (see Bender 1990; Koleva et al. 2008). In this work we are interested in the first two moments of the Gauss-Hermite parametrization. We tested whether our results vary for the two pPXF versions available and no significant differences were noticed when comparing  $1\sigma$  errors.

We test our measurement method by weighting the star particles' velocity according to their mass only. The recovered mass-weighted kinematics is very close to the intrinsic mass-weighted one, with the residuals being less than 5%.

## 4 RESULTS

### 4.1 Vertical velocity dispersion from the intrinsic mass-weighted kinematics

We calculate the vertical velocity dispersion of all the star particles of the simulation with a formation time  $t \geq t_{\text{in}}$  from the intrinsic mass-weighted kinematics as

$$\sigma_{z,t_{\text{in}}}^2 = \frac{\sum_{i=1}^{N_{t_{\text{in}}}} m_i v_{z,i}^2}{\sum_{i=1}^{N_{t_{\text{in}}}} m_i} \quad (1)$$

where  $N_{t_{\text{in}}}$  is the number of star particles in the given time range, while  $m_i$  and  $v_{z,i}$  are the mass and vertical velocity of  $i$ -th star particle, respectively.

When we consider all the simulation star particles at 10 Gyr,  $\sigma_z$  steadily increases from about 120 km s<sup>-1</sup> at 1 kpc from the centre to a maximum of about 270 km s<sup>-1</sup> at about 0.1 kpc. At smaller radii,  $\sigma_z$  drops to a central minimum value of about 220 km s<sup>-1</sup> (Figure 1). Since these are the intrinsic kinematics, the  $\sigma$ -drop is not an artefact due to the method we adopted in recovering the stellar kinematics. Moreover, the central dip in  $\sigma_z$  progressively fills in when removing star particles younger than 0.2, 0.4, . . . , 1.0, 1.5 Gyr. The radial profile of  $\sigma_z$  shows a central peak when all the stars younger than 2 Gyr are removed (Figure 1). Therefore, we infer that the central dip in  $\sigma_z$ , which we show below, and observe as a

$\sigma$ -drop in the recovered luminosity-weighted kinematics, is driven by the star formation of the galaxy centre.

To further investigate which stars contribute most to the  $\sigma$ -drop, we plot in Figure 2 the inner radial profile of  $\sigma_z$  and height  $z$  for stars of different age bins when the simulated galaxy is 6, 8 and 10 Gyr old. At 6 Gyr, the stars younger than 2 Gyr show an almost constant  $\sigma_z$  between about 0.3 and 0.5 kpc. Inwards it rises to a maximum of about 150 at about 0.1 kpc and drops to a central local minimum of 100 km s<sup>-1</sup>. The  $\sigma_z$  radial profile of the stars with an age between 2 and 4 Gyr and between 4 and 6 Gyr increases from about 150 km s<sup>-1</sup> at 0.5 kpc to about 300 and 350 km s<sup>-1</sup> in the centre, respectively. We interpret the larger  $\sigma_z$  measured for the older stellar populations due to the vertical heating of the stars, which also results in a notable increase of their scale height with time. The same trend is observed at 8 and 10 Gyr: younger stars are characterized by a remarkably lower  $\sigma_z$  with respect to the older ones and their  $\sigma_z$  radial profile has a pronounced central dip whereas older stars show a centrally peaked  $\sigma_z$ . The vertical heating of the stellar orbits is more effective in the first few Gyrs after formation. Afterwards both the shape and amplitude of the  $\sigma_z$  radial profile changes slowly with time. These findings confirm that younger stars play a crucial role in shaping the intrinsic mass-weighted kinematics in the centres of galaxies. We expect to observe an even stronger effect on the recovered luminosity-weighted kinematics since the younger stars are much brighter than the older ones. The vertical heating of the stellar orbits is also clear when we analyse the height,  $z_{rms}$ , which increases as a function of time, as expected. Therefore the stars first settle into a thin disc, which becomes progressively thicker with time.

Figure 3 shows an edge-on view of the spatial distribution of the simulated galaxy at 10 Gyr. The blue contours identify the population with  $t \leq 2$  Gyr that is responsible for the  $\sigma$ -drop.

### 4.2 LOS kinematic parameters from the recovered luminosity-weighted kinematics

In Figure 4 we compare the maps of the intrinsic mass-weighted kinematics (left-hand panels) to those measured from the spectral regions of the Mg I (middle panels) and Ca II (right-hand panels) triplets (luminosity-weighted kinematics). The galaxy is 10 Gyr old and is seen at an inclination  $i = 45^\circ$ . As anticipated, we find a pronounced  $\sigma$ -drop in the recovered kinematics which is even deeper than that in the intrinsic kinematics.

In Figure 5 we plot the residual maps we obtained by subtracting the recovered luminosity-weighted kinematics from the intrinsic mass-weighted one and dividing the difference by the intrinsic one to highlight the differences in the LOS kinematic parameters due to the adopted spectral range. The strongest fractional velocity residuals are along the minor-axis direction, when the intrinsic value is close to 0 km s<sup>-1</sup>. We find a good agreement in the velocity and velocity dispersion maps: the differences between the intrinsic and the recovered kinematics are compatible with the error bars, as visible in Figure 6 (right-hand panel).

We extract the radial profiles of LOS kinematic parameters from both the recovered and intrinsic kinematics in a 0.15-kpc wide strip along the major axis of the galaxy at 10 Gyr ( $i = 45^\circ$ ) and plot them in Figure 6. We decrease the bin sizes of the central regions to highlight the kinematics in that area. The intrinsic deprojected rotation curve rises to a maximum of about 220 km s<sup>-1</sup> at about 1 kpc from the centre and remains almost flat outwards, whereas the recovered rotation velocity is characterized by a peak velocity of about 300 km s<sup>-1</sup> at about 0.5 kpc and gently decreases to match



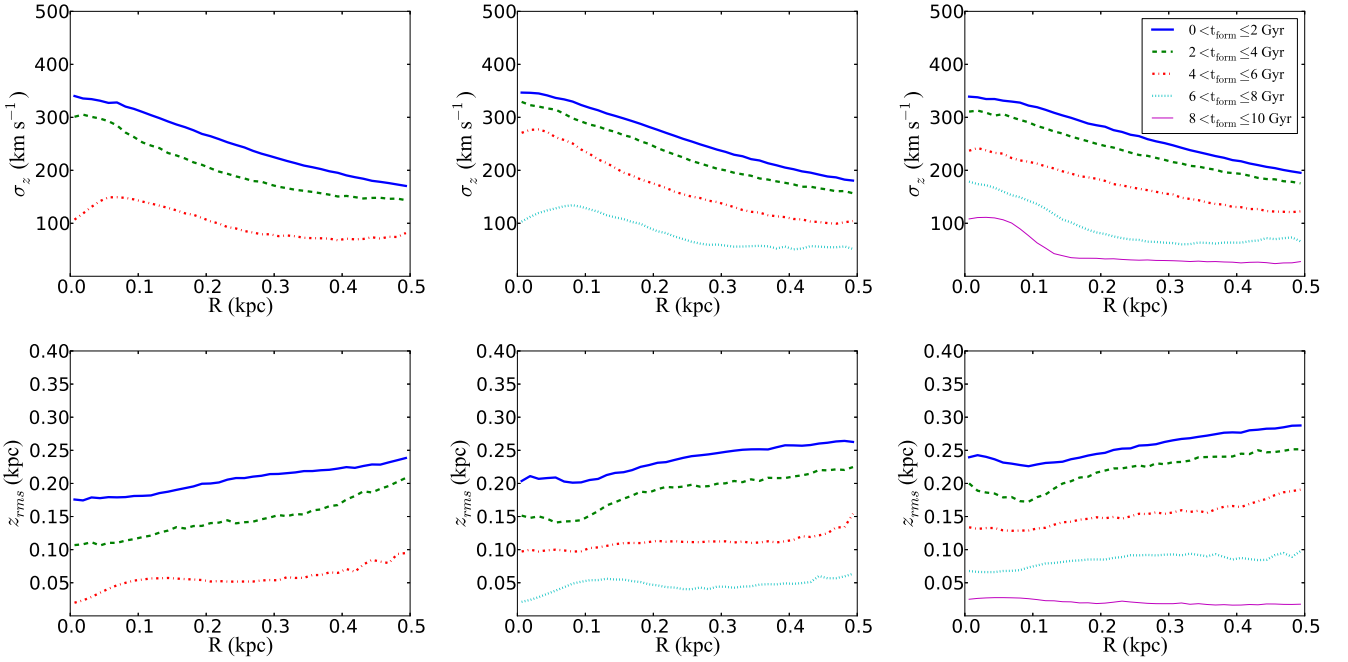


**Figure 2.** Radial profile of the vertical velocity dispersion  $\sigma_z$  (top panels), and  $rms$  height  $z_{rms}$  (bottom panels), measured from the intrinsic mass-weighted kinematics and density distribution as a function of the age of the star particles after 6 (left-hand panels), 8 (central panels), and 10 Gyr (right-hand panels). The coloured lines correspond to the profiles for stars formed at different times as indicated in the top right corner of the right-hand panel. The same colour marks the vertical velocity dispersion of the same stellar population evolving with time.

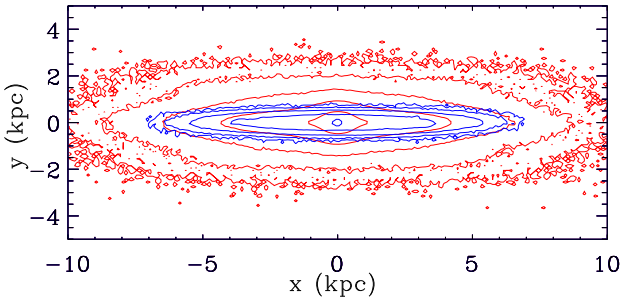


**Figure 3.** Density contours of the galaxy at 10 Gyr as seen edge-on. The blue contours identify the distribution of young stars (age  $\leq 2$  Gyr), which is responsible for the  $\sigma$ -drop, while the red ones are for older star particles. A colour version of this figure is available online.

the intrinsic velocity at about 2.5 kpc. The intrinsic velocity dispersion shows a central local minimum at about  $220 \text{ km s}^{-1}$ . It rises to about  $270 \text{ km s}^{-1}$  at about 0.2 kpc and then it decreases almost exponentially outwards. In the inner 0.5 kpc the recovered velocity dispersion flattens at about  $200 \text{ km s}^{-1}$  with a central sharp drop to about  $100 \text{ km s}^{-1}$ . The radial profiles of the intrinsic and recovered velocity dispersion profiles are very different also in the outer regions where the recovered velocity dispersion shows a marked decline to about  $50 \text{ km s}^{-1}$  at about 1 kpc and flattens out at larger radii. The same LOS kinematic features are observed along the galaxy major axis when it is 5 Gyr old (Figure 6). Indeed the intrinsic mass-weighted and recovered luminosity-weighted kinematics are remarkably similar to those extracted from the 10 Gyr simulation time-step. In particular, the  $\sigma$ -drop is clearly visible and more pronounced in the velocity dispersion profile obtained from the recovered luminosity-weighted kinematics.

To investigate the possibility that the recovered kinematics at the galaxy centre are biased to higher rotation velocities and lower velocity dispersions due to the presence of young stars in a thin and kinematically-cool nuclear disc, we show in Figure 7 the LOS kinematics of stars of different ages. This analysis demonstrates that young stars exhibit a significantly lower velocity dispersion and their rotation velocity is systematically higher than the oldest counterpart, which instead shows a peaked distribution of the velocity dispersion. Furthermore, there are no significant differences between the kinematics recovered in the two spectral ranges of Mg I and Ca II triplets for the stars in the same age bin.

A centrally-peaked profile is measured in the velocity dispersion of all the age bins. The central value increases from  $\approx 100 \text{ km s}^{-1}$  for the stars younger than 2 Gyr, to  $\approx 200 \text{ km s}^{-1}$  for the 2 – 4 Gyr-old stars and to  $\approx 300 \text{ km s}^{-1}$  for the stars older than 4 Gyr. The velocity dispersion profile is quite flat in the centre for stars younger than 2 Gyr and it shows two symmetric local maxima or bumps for stars with age between 0– and 6 and 6– and 10 Gyr, respectively. They correspond to the local minima observed in the rotation velocity curves, which all follow the same double-hump profile. This is characterized by an inner steep slope of the rotation velocity, reaching a local maximum followed by a slight drop to a local minimum. At larger radii the rotation velocity of all the age bins rises again, reaches an absolute maximum and then declines smoothly to match the intrinsic rotation velocity at 2.5 kpc. The recovered rotation curve from all the stars of the galaxy is rising out almost linearly to about 0.6 kpc with a small change in slope seen in the kinematics recovered in the Mg I spectral range. We conclude that both the shoulder of the rotation curve and the central drop of the velocity dispersion profile measured in the recovered kinematics are due to the younger stars.

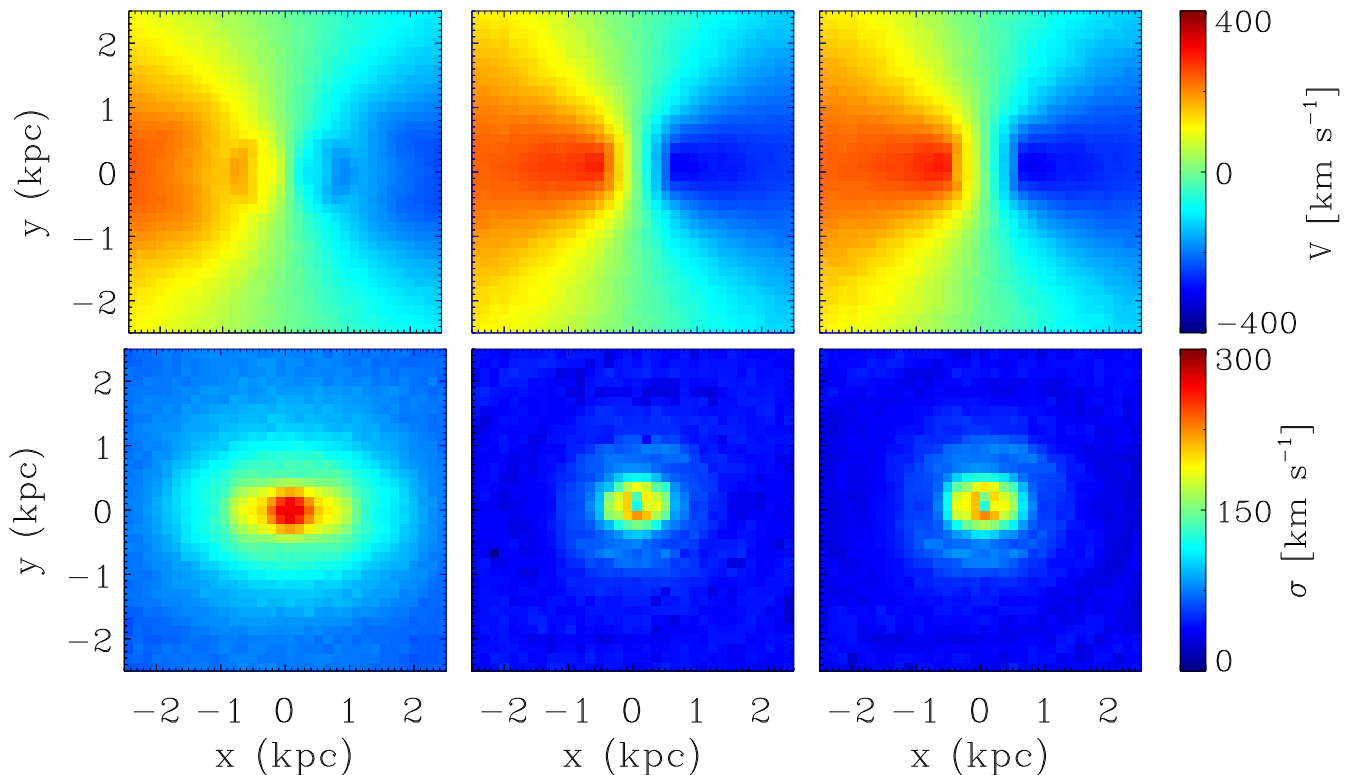


**Figure 4.** Intrinsic mass-weighted kinematics (left-hand panels) and recovered luminosity-weighted kinematics measured in the spectral range covering the Mg I (central panels) and Ca II triplets (right-hand panels) for the stars of the galaxy at 10 Gyr seen at an inclination of  $45^\circ$ . The LOS velocity (top panels) and velocity dispersion (bottom panels) are shown with the corresponding colour code at right.

## 5 DISCUSSION AND CONCLUSIONS

We have studied in detail the stellar kinematics of an unbarred galaxy with a high-resolution  $N$ -body + SPH simulation. The intrinsic kinematics are obtained by weighting the velocity of the star particles with their mass and are compared with the luminosity-weighted ones that we recover from synthetic spectra built by using our code SYNTRA, which combines the outputs of the simulation at different time-steps with stellar population synthesis models by Bruzual & Charlot (2003) to generate close-to-real spectroscopic data. We measured the luminosity-weighted stellar kinematics in two wavelength ranges covering the Mg I triplet at  $\lambda$  5164, 5173, 5184 Å and the Ca II triplet at  $\lambda$  8498, 8542, 8662 Å, without finding any substantial difference in the LOS velocity and velocity dispersion maps.

We notice remarkable differences in the rotation velocity curves and velocity dispersion profiles of the recovered luminosity-weighted and intrinsic mass-weighted kinematics. We demonstrate that observational data are biased by the presence of young stars in a nuclear disc. In our simulation such a disc is thin and kinematically cool and the complex kinematics in the central regions are a result of the superposition of older and younger stars. This should not be confused with the nuclear stellar discs, which are found in the centre of many galaxies, with scale-lengths  $\approx 10$ – $50$  pc and luminosities  $L_V \approx 10^6$ – $10^7 L_\odot$  (Pizzella et al. 2002; Morelli et al. 2010; Corsini et al. 2016), which are the smallest and brightest stellar discs known to date when compared to the embedded discs of early-type galaxies ( $h \approx 100$  pc) and to the main discs of lenticular and spiral galaxies (van den Bosch, Jaffe, & van der Marel 1998). The young disc found in the simulation can be better associated

with a pseudobulge, because it is characterized by different co-existing components (Fabricius et al. 2012; Méndez-Abreu et al. 2014; de Lorenzo-Cáceres et al. 2012). The total mass of the young stars ( $t \leq 2$  Gyr) represents 10% of the total mass of all the star particles, while it contributes up to 50% to the total luminosity. The SFR of the young population is  $1.1 M_\odot \text{ yr}^{-1}$ , in good agreement with the findings of other studies (Wozniak et al. 2003; Wozniak & Champavert 2006).

We find a significant drop in the velocity dispersion profile in our recovered luminosity-weighted kinematics, much more than that in the intrinsic mass-weighted one. In the simulation the inflow of gas to the central region of the galaxy creates a thin kinematically cool disc where stars form, reducing the central velocity dispersion. The fact that the  $\sigma$ -drop is more pronounced in the luminosity-weighted kinematic maps is a clear sign that the younger stars dominate the light distribution in the centre, although their contribution to the galaxy mass is less significant. This result demonstrates that a younger, luminous but not massive stellar population can bias the recovered gravitational potential of galaxies when weighted by luminosity. The visibility of  $\sigma$ -drops strongly depends on the mass ratio between the old dynamically-hot population and the young dynamically-cool one. This finding is extremely important to correctly interpret the kinematics of the central regions of galaxies, such as for the derivation of black hole masses using stellar kinematics. In our case, the  $\sigma$ -drop is linked to the presence of a central disc, as is clear from the double-hump shape of the rotation velocity curve.

Integral field spectroscopy of nearby galaxies can probe the full extent and amplitude of  $\sigma$ -drops and to which stellar com-

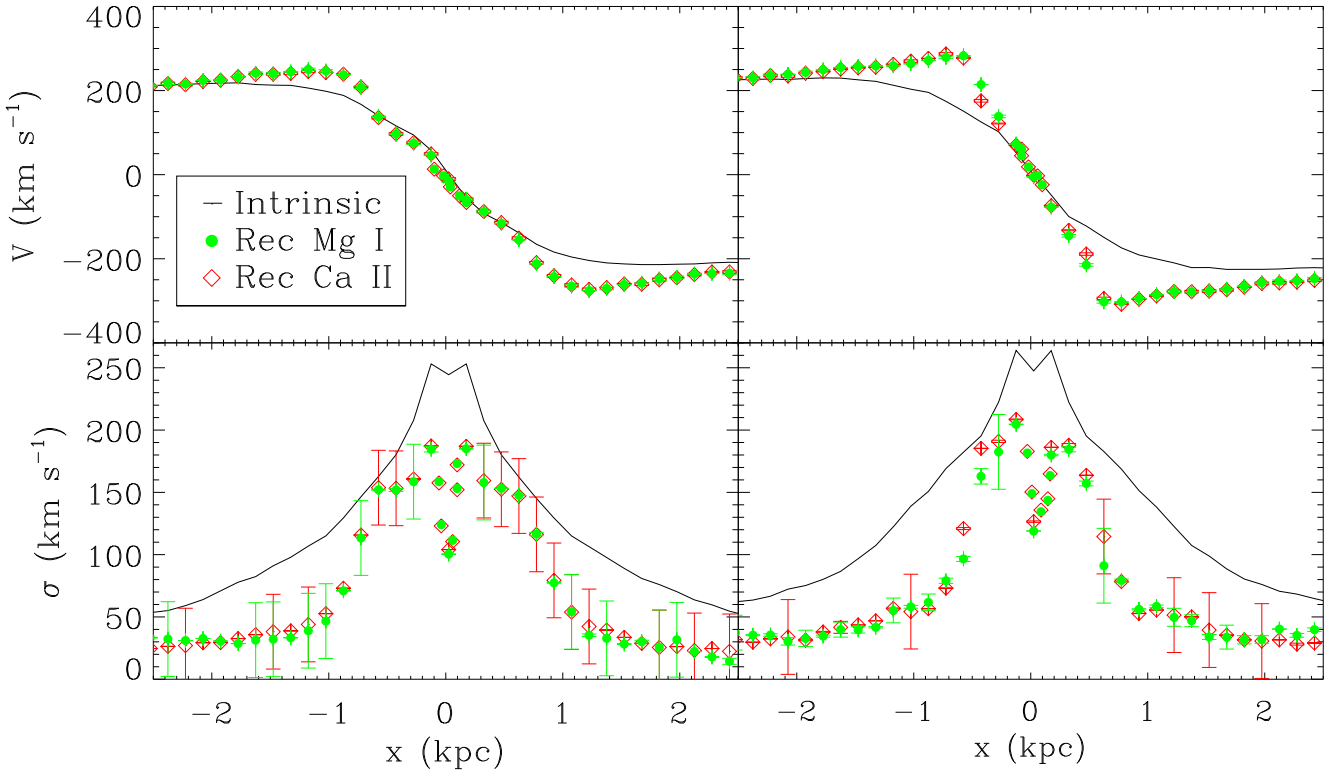


**Figure 6.** Intrinsic mass-weighted kinematics (solid black lines) and recovered luminosity-weighted kinematics measured in the spectral ranges covering the Mg I (green circles) and Ca II triplets (red triangles) along the major axis of the simulated galaxy at 5 Gyr (left-hand panels) and 10 Gyr (right-hand panels) seen at an inclination of  $45^\circ$ . The radial profiles of the LOS velocity are shown at top and velocity dispersion are shown at bottom.

ponent they are associated, providing information on the current stellar populations and their star formation history. In this sense,  $\sigma$ -drops can shed light on to the current dynamical state of galaxy central regions. In this context, we highlight that our code SYNTRA represents an extremely useful tool for building mock observations that can be used to recover luminosity-weighted kinematics and analyse simulations that include multiple stellar populations, for example kinematic cores and counter-rotating discs, but also galaxies with both thick and thin disc components. We would be able to disentangle the contribution of these components and compare simulation results with those found in recent integral-field spectroscopic surveys, such as ATLAS3D (Cappellari et al. 2011) and CALIFA (Mármol-Queraltó et al. 2011).

## 6 ACKNOWLEDGEMENTS

EP acknowledges the Jeremiah Horrocks Institute of the University of Central Lancashire for the hospitality while this paper was in progress. EP was partially supported by Accademia Nazionale dei Lincei and Fondazione Ing. Aldo Gini. Additional support while the paper was completed was provided by the Italian Ministry for Education University and Research (MIUR). VPD was supported by STFC Consolidated grants no. ST/J001341/1 and no. ST/M000877/1. VPD acknowledges being a part of the network supported by the COST Action TD1403 “Big Data Era in Sky and Earth Observation”. DRC was supported by STFC Consolidated grant no. ST/J001341/1. EMC, EDB, LM, and AP are supported by Padua University through grants 60A02-5857/13, 60A02-5833/14, and 60A02-4434/15 and BIRD 164402/16. The simulation was run

at the DiRAC Shared Memory Processing system at the University of Cambridge, operated by the COSMOS Project at the Department of Applied Mathematics and Theoretical Physics on behalf of the STFC DiRAC HPC Facility ([www.dirac.ac.uk](http://www.dirac.ac.uk)). This equipment was funded by BIS National E-infrastructure capital grant ST/J005673/1, STFC capital grant ST/H008586/1, and STFC DiRAC Operations grant ST/K00333X/1. DiRAC is part of the National E-Infrastructure. EP would like to thank R. Ragazzoni for his support while this work was in progress.

## REFERENCES

- Athanassoula E., Misiriotis A., 2002, MNRAS, 330, 35
- Bender R., 1990, A&A, 229, 441
- Bertelli G., Bressan A., Chiosi C., Fagotto F., Nasi E., 1994, A&AS, 106,
- Bertola F., Cinzano P., Corsini E. M., Pizzella A., Persic M., Salucci P., 1996, ApJ, 458, L67
- Binney J., 1980, MNRAS, 190, 873
- Bottema R., 1989, A&A, 221, 236
- Bottema R., Gerritsen J. P. E., 1997, MNRAS, 290, 585
- Bruzual G., Charlot S., 2003, MNRAS, 344, 1000
- Bureau M., Athanassoula E., 2005, ApJ, 626, 159
- Cappellari M., Emsellem E., 2004, PASP, 116, 138
- Cappellari M., et al., 2011, MNRAS, 413, 813
- Chung A., Bureau M., 2004, AJ, 127, 3192
- Ciotti L., Lanzoni B., 1997, A&A, 321, 724
- Coccolo L., et al., 2015, A&A, 581, A65

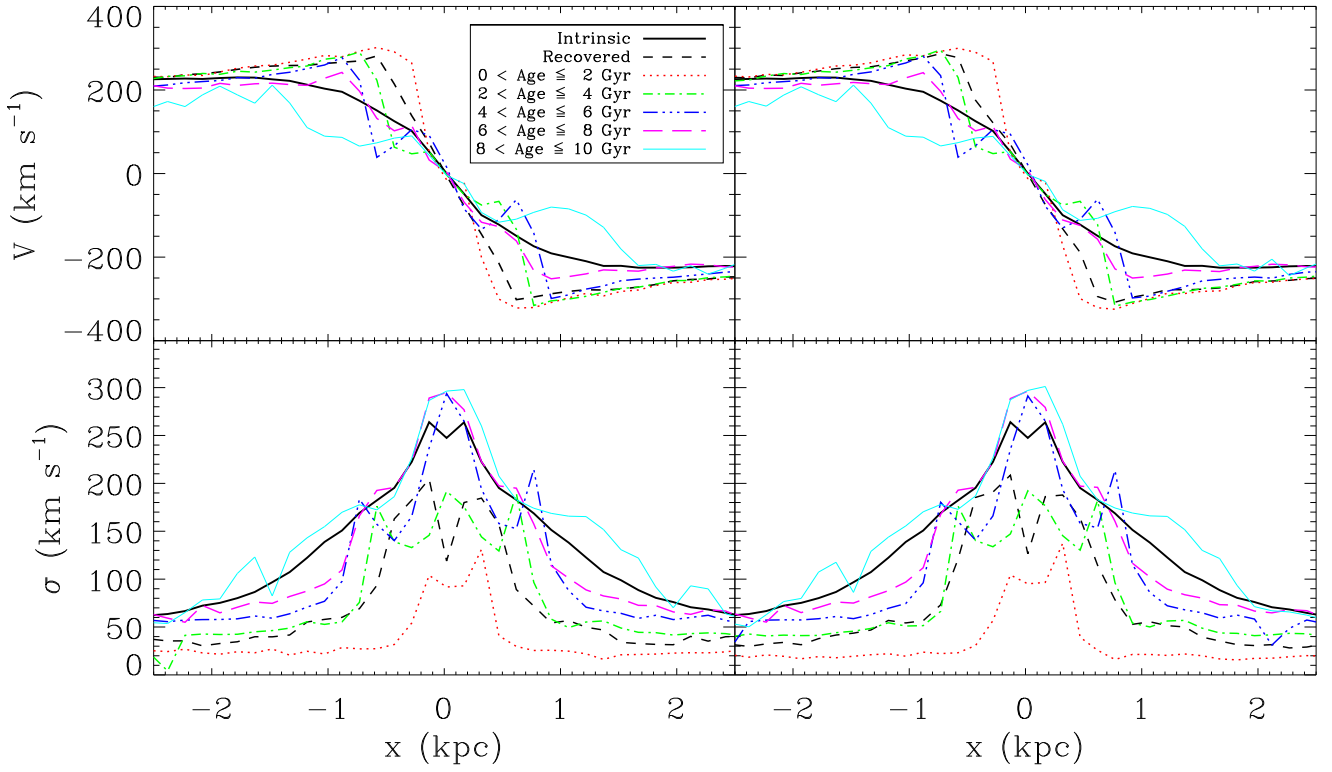


**Figure 7.** The radial profiles of the LOS velocity and velocity dispersion (from top to bottom) along the major axis of the simulated galaxy at 10 Gyr seen at an inclination of  $45^\circ$  for stars of different age (solid colour lines coded as indicated in the left-hand panel) from the kinematics recovered in the spectral ranges covering the Mg I triplet lines (left-hand panels) and Ca II triplet (right-hand panels). The solid and dashed black lines correspond to the recovered luminosity-weighted and intrinsic mass-weighted kinematics obtained including all the simulation star particles, respectively.

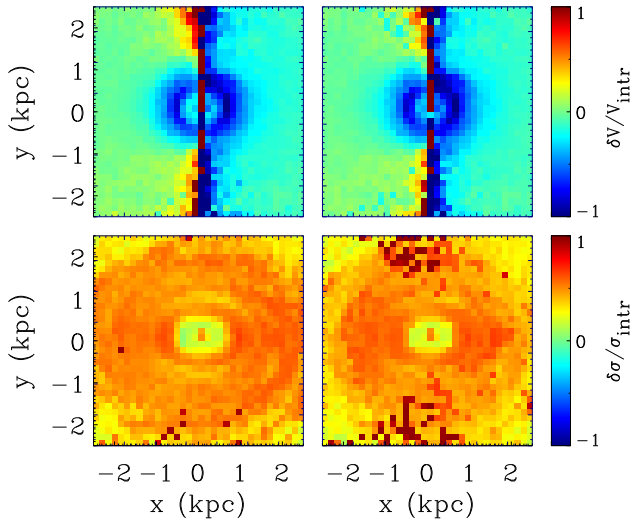


**Figure 5.** Maps of the residuals of the recovered luminosity-weighted kinematics measured in the spectral range covering the Mg I (left-hand panels) and Ca II triplets (right-hand panels) with respect to the intrinsic mass-weighted kinematics for the stars of the simulated galaxy at 10 Gyr seen at an inclination of  $45^\circ$ . The residuals of the LOS velocity (top panels) and velocity dispersion (bottom panels) are shown with the corresponding colour code at the right. The size and orientation of the field of view are the same as in Figure 4.

- Cole D. R., Debattista V. P., Erwin P., Earp S. W. F., Roškar R., 2014, *MNRAS*, 445, 3352  
 Comerón S., Knapen J. H., Beckman J. E., 2008, *A&A*, 485, 695  
 Corsini E. M., Morelli L., Pastorello N., Dalla Bontà E., Pizzella A., Portaluri E., 2016, *MNRAS*, 457, 1198  
 de Lorenzo-Cáceres A., Vazdekis A., Aguerri J. A. L., Corsini E. M., Debattista V. P., 2012, *MNRAS*, 420, 1092  
 Dressler A., Richstone D. O., 1990, *ApJ*, 348, 120  
 Emsellem E., Greusard D., Combes F., Friedli D., Leon S., Pécontal E., Wozniak H., 2001, *A&A*, 368, 52  
 Erwin P., et al., 2015, *MNRAS*, 446, 4039  
 Fabricius M. H., Saglia R. P., Fisher D. B., Drory N., Bender R., Hopp U., 2012, *ApJ*, 754, 67  
 Fabricius M. H., et al., 2014, *MNRAS*, 441, 2212  
 Falcón-Barroso J., et al., 2006, *MNRAS*, 369, 529  
 Friedli D., 1996, *A&A*, 312, 761  
 Gerhard O. E., 1993, *MNRAS*, 265, 213  
 Graham A. W., Colless M. M., Busarello G., Zaggia S., Longo G., 1998, *A&AS*, 133, 325  
 Jarvis B. J., Dubath P., Martinet L., Bacon R., 1988, *A&AS*, 74, 513  
 Koleva M., Prugniel P., De Rijcke S., 2008, *AN*, 329, 968  
 Krajnović D., et al., 2008, *MNRAS*, 390, 93  
 Krajnović D., et al., 2013, *MNRAS*, 433, 2812  
 Loebman S. R., Roškar R., Debattista V. P., Ivezić Ž., Quinn T. R., Wadsley J., 2011, *ApJ*, 737, 8  
 Mármol-Queraltó E., et al., 2011, *A&A*, 534, A8  
 Méndez-Abreu J., Debattista V. P., Corsini E. M., Aguerri J. A. L., 2014, *A&A*, 572, 25



- Miller G. E., Scalo J. M., 1979, *ApJS*, 41, 513
- Morelli L., Cesetti M., Corsini E. M., Pizzella A., Dalla Bontà E., Sarzi M., Bertola F., 2010, *A&A*, 518, A32
- Pizzella A., Corsini E. M., Morelli L., Sarzi M., Scarlata C., Stivavelli M., Bertola F., 2002, *ApJ*, 573, 131
- Pérez I., Sánchez-Blázquez P., Zurita A., 2009, *A&A*, 495, 775
- Raiteri C. M., Villata M., Navarro J. F., 1996, *A&A*, 315, 105
- Salpeter, E. E., 1955, *ApJ*, 121, 161
- Shen J., Rich R. M., Kormendy J., Howard C. D., De Propris R., Kunder A., 2010, *ApJ*, 720, L72
- Stinson G., Seth A., Katz N., Wadsley J., Governato F., Quinn T., 2006, *MNRAS*, 373, 1074
- van den Bosch F. C., Jaffe W., van der Marel R. P., 1998, *MNRAS*, 293, 343
- van der Marel R. P., Franx M., 1993, *ApJ*, 407, 525
- van der Marel R. P., 1994, *MNRAS*, 270, 271
- Wadsley J. W., Stadel J., Quinn T., 2004, *NewA*, 9, 137
- Weidemann V., 1987, *A&A*, 188, 74
- Woosley S. E., Weaver T. A., 1995, *ApJS*, 101, 181
- Wozniak H., Combes F., Emsellem E., Friedli D., 2003, *A&A*, 409, 469
- Wozniak H., Champavert N., 2006, *MNRAS*, 369, 853